ORIGINAL RESEARCH ARTICLE

Interfacial Segregation of Fe and Si on TiB_2 Surface and Refinement of Fe-Bearing Intermetallic Compounds and Primary Si

Part I: Segregation Phenomenon and Formation of Two-Dimensional Compounds (2DCs) at the Al/TiB_2 Interface

ZHONGPING QUE, YUN WANG, ZHONGYUN FAN,
RALUCA FLORENTINA NEGREA, XIAORONG ZHOU, and QUENTIN RAMASSE

Al–Ti–B-based grain refiners have been successfully used in the aluminium industry for more than six decades. Recent advancements have demonstrated that manipulating the nucleation potency of substrates through interfacial segregation can enhance the heterogeneous nucleation of both single-phase and intermetallic compounds by providing structural and compositional templating. However, the segregation of Fe and Si, two of the most common alloying elements or impurities in Al alloys, on TiB_2 surface and its subsequent effects are not fully understood. In this work, TiB_2 particles were synthesized in an Al–3.7Ti–1.5B alloy melt containing 0.43 wt pct excess free Ti, followed by isothermal treatment to promote Fe and Si segregation on the TiB_2 surface. The segregation behaviour of Fe and Si on different terminated surfaces of the TiB_2 particles was investigated using scanning transmission electron microscopy (STEM). The experimental results show that Fe and Si exhibit distinct segregation behaviours depending on the atomic configuration of TiB_2 surfaces, leading to the formation of two-dimensional compounds (2DCs) at the Al/TiB_2 interfaces. The formation of interfacial segregation layers has been shown to profoundly affect subsequent solidification, particularly nucleation and growth processes of intermetallic compounds (IMCs) in the alloys, resulting in significant refinement of these phases and the final solidification microstructure. In part 1, this research focuses on investigating the nature of interfacial segregation of Fe and Si on TiB_2 particles. Experimental results concerning the segregation and the characterization of the structure and chemistry of the resulting interfacial layers are presented. In the subsequent Part II, the investigation will address the effects of Fe and Si interfacial segregation on the solidification behaviour of Al alloys, with particular emphasis on the heterogeneous nucleation and refinement of primary Fe-bearing intermetallic compounds and the primary Si phase in Al–Fe–Si and Al–Si alloys.

ZHONGPING QUE, YUN WANG, ZHONGYUN FAN, and RALUCA FLORENTINA NEGREA are with the Brunel Centre for Advanced Solidification Technology (BCAST), Brunel University London, Uxbridge, Middlesex UB8 3PH, UK. Contact e-mail: Zhongping.Que@brunel.ac.uk XIAORONG ZHOU is with the School of Materials, University of Manchester, Manchester M13 9PL, UK. QUENTIN RAMASSEIS with the SuperSTEM Laboratory, SciTech Daresbury Campus, Daresbury WA4 4AD, UK.
Manuscript submitted July 22, 2025; accepted August 27, 2025.

Published online: 12 September 2025

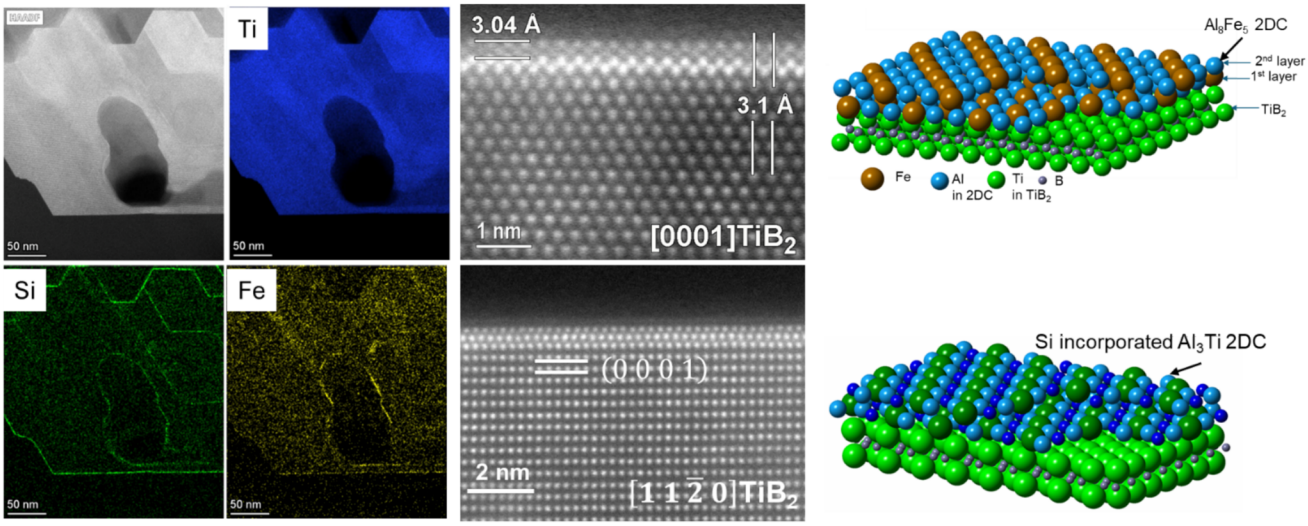

https://doi.org/10.1007/s11661-025-07970-7

I. INTRODUCTION

GRAIN refinement is critical in metal casting as it helps reduce casting defects and achieve superior mechanical properties. Effective grain refinement can also reduce or eliminate the need for subsequent processes such as thermo-mechanical deformation and heat treatment, resulting in energy savings and reduced greenhouse gas emissions. Numerous approaches to achieving grain refinement in Al alloys have been developed over the past several decades, including chemical methods,[1–5] thermal control,[6] and mechanical methods.[7] Currently, chemical inoculation, specifically, the addition of external grain refiners such as Al–Ti–B, is one of the most effective strategies for grain refinement in Al alloys. The mechanism of grain refinement is usually understood in terms of enhanced heterogeneous nucleation facilitated by potent nucleation particles, along with restricted grain growth due to alloying elements.[3,8–11]

Having been widely used in Al alloys for many decades, Al–Ti–B-based grain refiners are effective in refining α-Al grains.[12–16] The mechanisms involved in nucleation and grain refinement through the addition of TiB_2 particles have been extensively investigated, with various experimental evidence gathered over the past few decades.[11–16] Recent studies have shown that the refinement of α-Al grains is attributed to the enhanced nucleation of α-Al on Al_3Ti 2DC layer formed on (0 0 0 1) TiB_2 surface through Ti interfacial segregation. This process significantly reduces the misfit between α-Al and TiB_2 particles, thereby improving the nucleation potency of TiB_2 substrates.[3,17] In recent years, theories of heterogeneous nucleation have rapidly evolved, informed by new insights from various perspectives, including pre-nucleation[18–20] and the effect of interfacial segregation at the solid/substrate interface.

Experiments have revealed that interfacial segregation of solutes on the surface of solid particles in liquid metals usually leads to the formation of 2D interfacial layers.[17,21,22] For instance, alloying elements such as Si and Zr tend to segregate on the surface of TiB_2 particles, with the segregation behaviour depending on their concentration, processing temperature, and holding time. The formation of either 2DC or 2-dimensional solution (2DS) changes the nucleation potency of the TiB_2 particles and the variation in the potency is expected to either enhance or impede heterogeneous nucleation, as experimentally demonstrated by the positive effect of Ti segregation (formation of Al_3Ti 2DC)[3] and negative effect (so-called poisoning) of Zr (formation of Ti_2Zr 2DC)[21] and Si (formation of Si-rich 2DS) on nucleation of α-Al.[22]

Given the fact that Al–Ti–B master alloys are widely used in Al foundry industry, understanding of the interactions between some common alloying elements/impurities and TiB_2 particles is essential. This is particularly important for recycled Al alloys, which may contain a broader range of impurities at varying concentrations. The resilience of TiB_2 particles in achieving grain refinement in these recycled alloys is increasingly being tested. Little attention has been paid to interfacial segregation of Fe and Si which are the most common alloying elements or impurities in aluminium.

In this study, by synthesizing TiB_2 particles in Al–3.7Ti–1.5B master alloy with 1.5 wt pct Fe and 1.0 wt pct Si addition, interfacial segregation of Fe and Si on the TiB_2 particles were extensively examined using the high-resolution scanning transmission electron

microscopy (HR-STEM). The corresponding structural and compositional variations at the Al/TiB_2 interface due to the interfacial segregations have been comprehensively analysed.

In Part I of this study, we present experimental results on the interfacial segregation phenomena, segregation behaviour, and identification of the structure and chemistry of the resulting interfacial layers. In a separate Part II, we will show the impacts of the modified TiB_2 particles with Fe and Si interfacial segregations on heterogeneous nucleation of different phases in Al alloys, particularly focussing on the refinement of the Fe-bearing intermetallic compounds and the primary Si phase.

II. EXPERIMENTAL

A. *Synthesis of Borides*

TiB_2 particles were synthesized in-situ within an Al–Ti–B (nominal composition: 3.7 pct Ti and 1.5 pct B) alloy containing 0.43 pct excess Ti (All compositions are in wt pct unless specified otherwise). The Al–Ti–B alloy was produced by melting commercial-purity aluminium (CP-Al, > 99.86 pct Al) at 800 °C, followed by the sequential addition of Al–5B and Al–10Ti master alloys. The precise chemical compositions and impurity levels of the starting materials are listed in Table I. After the addition of the master alloys, the melt was held at 800 °C for a further 4 hours with continuous stirring to ensure complete mixing and to allow the synergistic reaction for TiB_2 particle formation to proceed to completion. The prepared Al–Ti–B alloy melt was separated into two different crucibles equally. One half was cast into thin sheets with 1 to 5 mm thickness in a steel mould.

To the other half of the melt, a certain amount of Al–38Fe and Al–50Si master alloys was added to achieve the targeted addition of 1.0 pct Fe and 1.0 pct Si addition, followed by holding at 800 °C for 4 hours. Stirring with a blender was applied to the new Al–Ti–B–Fe–Si alloy melt during the holding. Finally, the treated melt was cast into thin sheets in the same steel mould. The composition of the Al–Ti–B–Fe–Si alloy was measured using Inductively Coupled Plasma (ICP) analysis and the results are provided in Table I. Impurities such as Ni, Zn, and Mn were evidently introduced from the raw master alloys. The actual Fe concentration (1.5 pct) was higher than the nominal 1.0 pct, likely due to the inhomogeneous composition of the Al–Fe master alloy and the contribution of impurities from the Al–10Ti, Al–5B, and Al–50Si master alloys.

B. *Characterization*

The morphology and size distribution of the synthesized boride particles in the Al–3.7Ti–1.5B–1.5Fe–1.0Si master alloy were characterized using scanning electron microscopy (SEM) with a Zeiss Supra 35 instrument operated at an accelerating voltage between 5 and 20 kV.

For transmission electron microscopy (TEM) analysis, disc samples 3 mm in diameter were first mechanically ground to a thickness below 50 μm, then further thinned by argon ion milling. Ion thinning was performed using a Gatan Precision Ion Polishing System (PIPS) at an accelerating voltage of 1.0 to 5.0 kV with an incident beam angle of 3 to 5 deg.

To reveal interfacial segregation of elements on the TiB_2 particles, atomic-resolution scanning TEM (STEM) with Z-contrast high-angle annular dark-field (HAADF) imaging and energy-dispersive X-ray spectroscopy (EDS) mapping were carried out using an aberration (Cs)-corrected SPECTRA 300 TEM from ThermoFisher, equipped with Super-X EDS detector and operated at 200 kV. A convergence beam angle (α) of 15.7 mrad was employed, yielding a depth of focus (DoF) of approximately 10 nm, which optimized EDS signal acquisition. To enhance the signal-to-noise ratio in the EDS maps, the data were pre-processed using a Gaussian blur filter. A camera length (CL) of 91 mm was used, resulting in a high-angle annular dark-field (HAADF) detector collection angle (β) range of 72 to 200 mrad. Experimental HAADF-STEM images revealing Fe and Si segregation at the Al/TiB_2 interface were further analysed through simulated HAADF-STEM imaging using the commercial Tempas software package (Total Resolution LLC).

III. RESULTS

A. *Nature of Borides and the Interfacial Segregation in Al–3.7Ti–1.5B Master Alloy*

Figure 1(a) presents the hexagonal morphology of the synthesized boride particles in the Al–3.7Ti–1.5B alloy. The particles exhibit a tendency to agglomerate, with sizes ranging from several hundred nanometres to tens

Table I. Chemical Composition of the As-Cast Alloy (Wt Pct)

Alloy	Al	Si	Mg	Fe	Mn	Ti	Ni	Zn	Zr	B	Supplier
CP-Al	balance	< 0.04	—	< 0.06	—	—	—	—	—	—	Norton
Al–10Ti	balance	0.12	0.02	0.35	—	10.7	—	—	—	—	Affilips
Al–5B	balance	0.09	—	0.17	—	—	—	—	—	5.44	Aleastur
Al–27Si	balance	27.0	—	0.58	0.11	—	0.43	0.33	—	—	this work
Al–50Si	balance	50	0.01	0.39	0.02	0.04	0.01	0.02	—	—	Avon
Al–3.7Ti–1.5B–1Fe−1Si Alloy	balance	1.0	0.1	1.5	0.1	3.7	0.6	0.3	0.1	1.5	this work

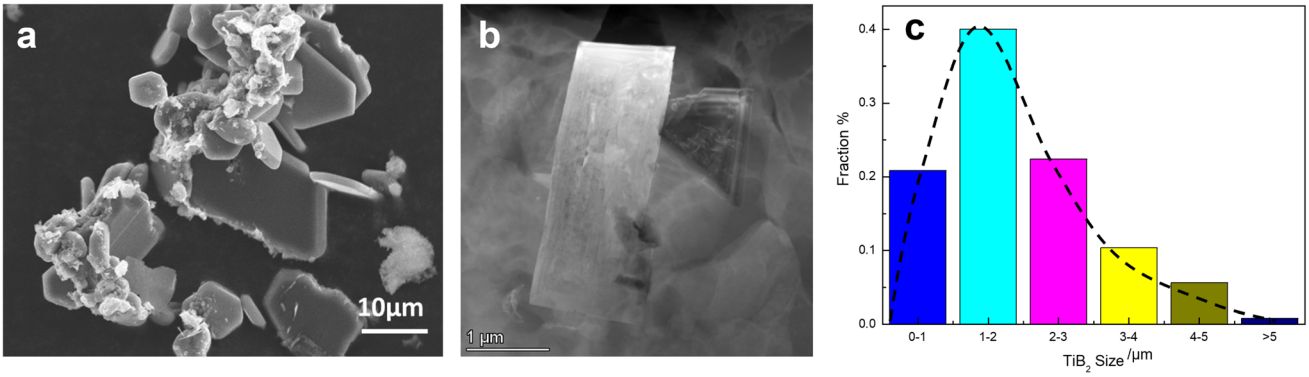

Fig. 1—(*a*) Scanning electron microscopy (SEM) image showing the 3-dimentional (3D) hexagonal morphology of the boride particles in Al–3.7Ti–1.5B–1.5Fe–1.0Si master alloy; (*b*) TEM image showing a 2D rectangle morphology of boride particles; and (*c*) the size distribution of the boride particles.

of micrometres. The thickness of the particles varies from several hundred nanometres to about 1 micrometre. The majority of the TiB_2 particles exhibit sizes in the range of 1 to 3 μm, which corresponds to the dominant particle population. Figure 1(a) presents the three-dimensional morphology of the TiB_2 particles; however, it should be noted that many of the smaller particles are lost during the etching process, and therefore this image does not fully capture the entire size distribution. To clarify this distinction, an additional 2D morphology image is included in Figure 1(b). The quantitative size analysis shown in Figure 1(c) is based on two-dimensional morphologies, which provide a more representative measurement of particle sizes. Fe and Si segregation was repeatedly observed at the interfaces of the Al/TiB_2 by STEM imaging and EDS mapping, as shown in Figures 2 and 3. Figure 2 presents an EDS analysis of a TiB_2 particle oriented along the $[0\,0\,0\,1]$ direction, which is predominantly surrounded by Si, with localized regions containing Fe, as shown in the Si and Fe EDS maps. It is also evident that Fe segregation at the Al/$(1\,0\,\bar{1}\,0)$ TiB_2 interface is not uniform: certain regions display pronounced segregation, while others show weaker enrichment. In comparison with Fe segregation at the AlB_2 interface,[22] the segregation on TiB_2 is less pronounced. Figure 2(g) presents the intensity profile extracted along the green arrow and averaged over the area marked by the green rectangle at the Al/$(1\,0\,\bar{1}\,0)$ TiB_2 interface, revealing the segregation of both Fe and Si. Strong Fe and Si signals are also detected within the TiB_2 particle [Figure 2(a)], which can be attributed to internal defects and terminated faceted planes. These internal planes behave in a manner similar to external facets, providing sites where Fe and Si segregation can occur. Figure 2(g) presents a HAADF image processed with Gaussian blur filtering, in which the 2DC layers can be more clearly distinguished. The image reveals different 2DC layer structures at the $\{1\,0\,\bar{1}\,0\}$ faceted planes, reflecting variations in segregation levels that may be related to factors such as Fe concentration in the master alloy and segregation time.

Figure 3(a) is a HAADF-STEM image viewed along the $[1\,1\,\bar{2}\,0]$ direction of the boride particle which terminated with $(0\,0\,0\,1)$ and $(\bar{1}\,1\,0\,0)$$TiB_2$ surface. The Ti elemental map in Figure 2(e) clearly demonstrates that although there are variations in Ti content from the surface towards the centre of the boride particle, the surface is predominantly terminated with TiB_2 rather than AlB_2. Figure 3(d) shows that Si segregation covers both the Al/$(0\,0\,0\,1)$ and Al/$(\bar{1}\,1\,0\,0)$$TiB_2$ surface. Fe was detected only at Al/$(\bar{1}\,1\,0\,0)$ TiB_2 interfaces and co-segregated with Si, Figures 3(f) and (h). In addition, Figure 3(e) shows internal variations of Ti and Al within the TiB_2 particles, which are likely attributable to local compositional fluctuations during particle growth, preceding the segregation of Fe and Si.

The intensity profile extracted from the EDS maps of B, Si, and Fe at the Al/$(0\,0\,0\,1)$$TiB_2$ interface, as shown in Figure 3(g), revealed the segregation of Si only, without any Fe signal. Similarly, the intensity profile extracted from the EDS maps of B, Si, and Fe at the Al/$(\bar{1}\,1\,0\,0)$$TiB_2$ interface, shown in Figure 3(h), indicated the co-segregation of Fe and Si.

B. *Interfacial Segregation of Fe and Si at Al/*$(\bar{1}\,1\,0\,0)$*TiB₂ Interface*

The interfacial segregation at the Al/$(\bar{1}\,1\,0\,0)$$TiB_2$ interface was further investigated at atomic level with the HAADF-STEM imaging, as shown in Figure 4. Figure 4(a) shows a set of EDS mapping at the Al/$(\bar{1}\,1\,0\,0)$ TiB_2 interface, viewed along the $[1\,1\,\bar{2}\,0]$ direction. It shows the Fe and Si segregation at the Al/$(\bar{1}\,1\,0\,0)$ TiB_2 interface. Figure4(b) also shows a set of EDS mapping at the Al/$(\bar{1}\,1\,0\,0)$ TiB_2 interface, viewed along a different direction, *i.e.* the $[0\,0\,0\,1]$ zone. It is also seen that Si segregation area is slightly wider than that of Fe. Careful analysis of the EDS maps revealed that Fe segregation above the outermost Ti layer of TiB_2, while Si was detected slightly penetrating the TiB_2 beneath the Al/TiB_2 interface.

The segregation and the formation of the 2-dimensional compound (2DC) is uneven, with 2 to 3 distinct layers observed along the Al/$(\bar{1}\,1\,0\,0)$ TiB_2 interface. Figures 5(a) through (d) present the HAADF-STEM

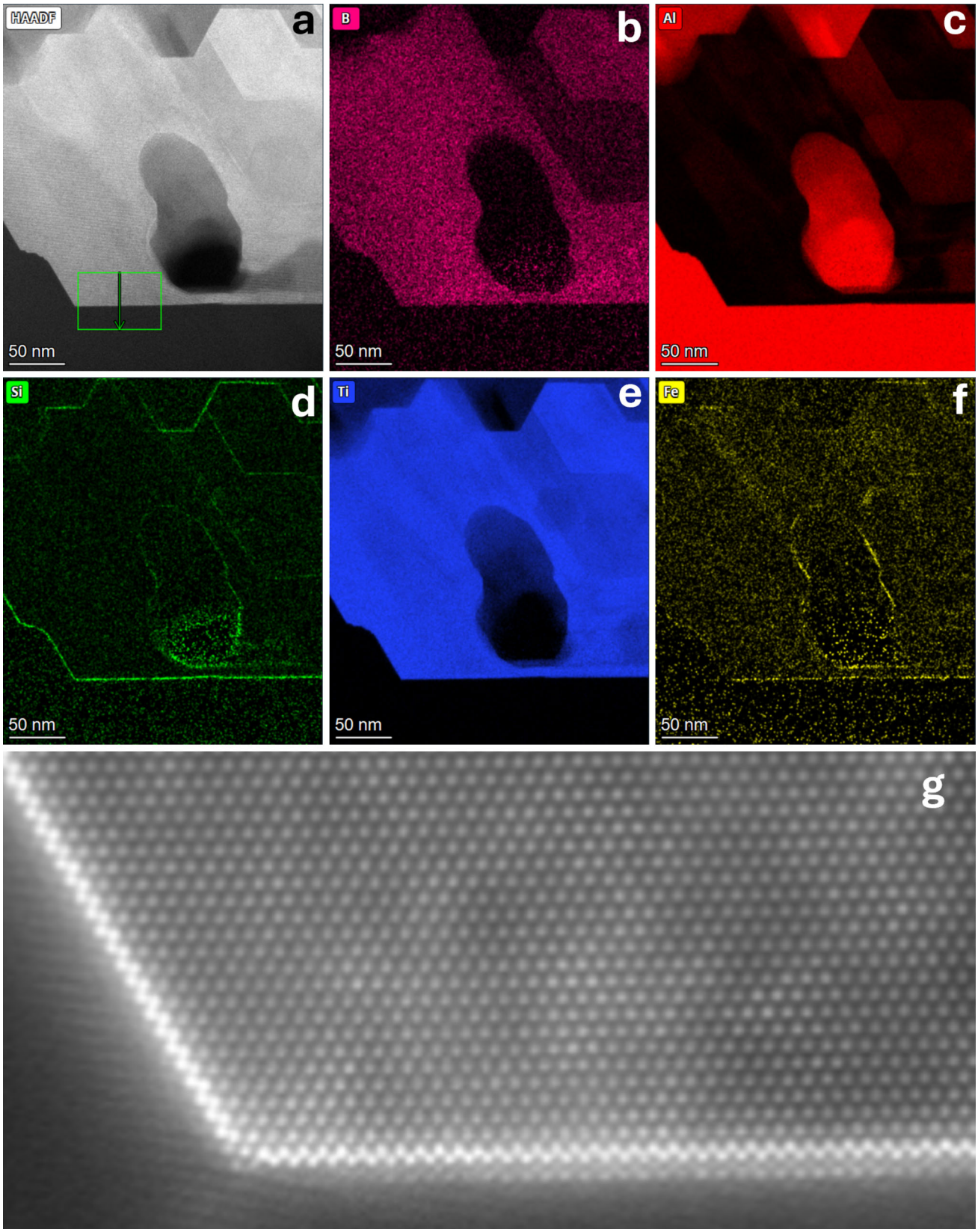

Fig. 2—Elemental segregation at the Al/TiB_2 interface in Al–3.7Ti–1.5B–1.5Fe−1.0Si alloy. (*a*) Low-magnification HAADF-STEM image of a TiB_2 particle viewed along the [0 0 0 1]TiB_2 zone axis, and (*b*) through (*f*) corresponding EDS maps of B, Al, Si, Ti, and Fe. The Si and Fe elemental maps show clear segregation at the Al/TiB_2 interface. (*g*) HAADF image that applied filtering techniques (Gaussian bluer), where the 2DC layers can be more clearly distinguished but presented different layers of 2DC at faceted planes (Color figure online).

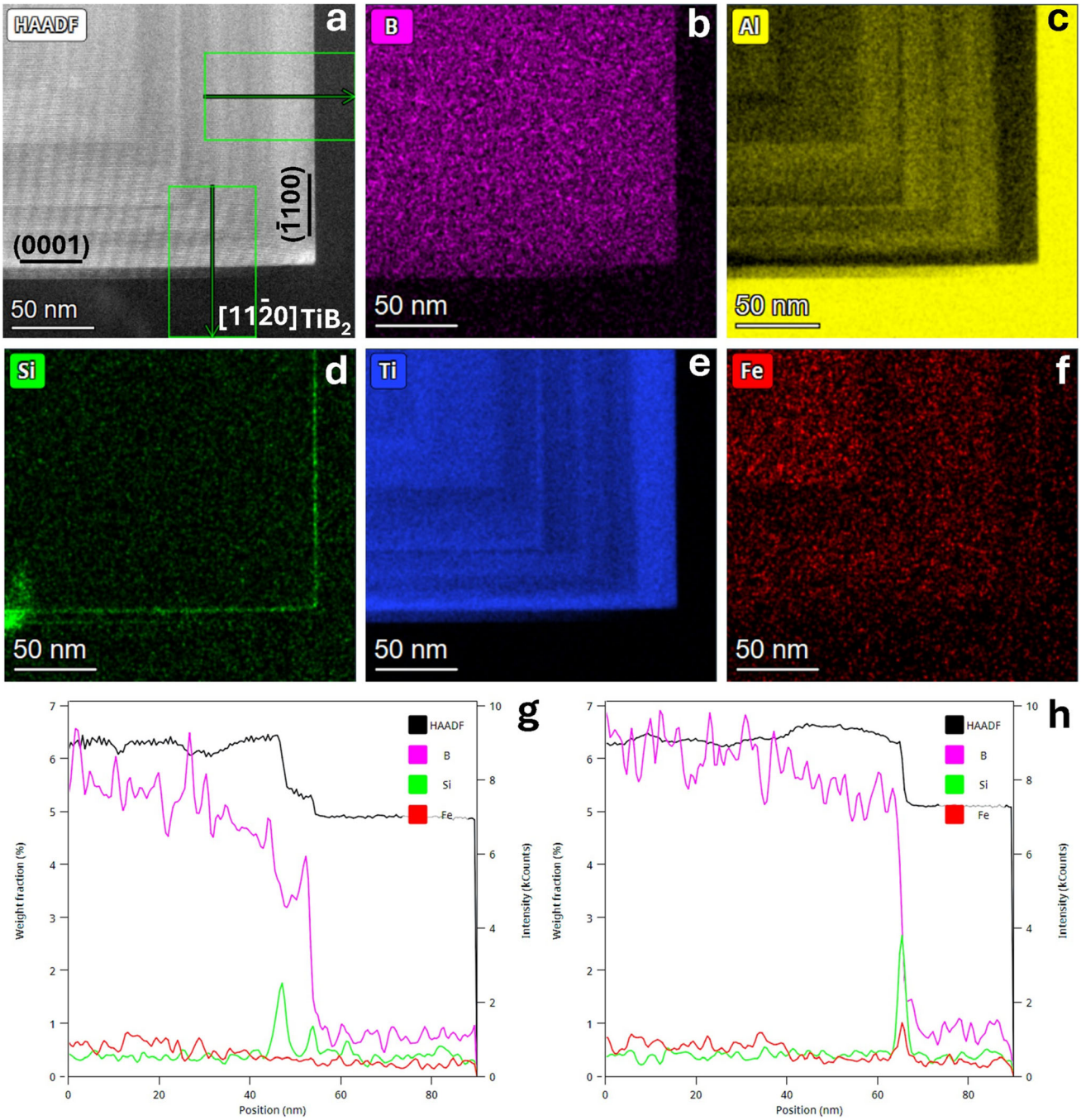

Fig. 3—Elemental segregation at the Al/TB_2 interface in Al–3.7Ti–1.5B–1.5Fe−1.0Si alloy. (*a*) HAADF-STEM image across the Al/TiB_2 interface, viewed along $[1\,1\,\bar{2}\,0]TiB_2$ direction, and (*b*) through (*f*) corresponding EDS elemental maps of (b) Ti (blue), (*c*) B (pink), (*d*) Al (red), (*e*) Si (green), and (f) Fe (yellow). The maps reveal Fe and Si segregation along the $(\bar{1}\,1\,0\,0)$ plane and Si segregation along the $(0\,0\,0\,1)$ plane of the TiB_2 particle. (*g*) and (*h*) Intensity profiles extracted from selected regions (green rectangles) along the (0 0 0 1) and $(\bar{1}\,1\,0\,0)$ surfaces of TiB_2 particle, respectively (Color figure online).

images showing the atomic arrangement at the Al/$(\bar{1}\,1\,0\,0)$ TiB_2 interface, viewed along the $[1\,1\,\bar{2}\,0]$ and $[0\,0\,0\,1]$ directions of TiB_2, respectively. Figure 5(a) shows that the number of atomic layers, whose atomic arrangement differs from that of TiB_2, above the top Ti layer of TiB_2 varies from two to three layers. In general, a two-layer structure is most commonly observed above the $(\bar{1}\,1\,0\,0)TiB_2$ surface, as illustrated in Figure 5(b). The atomic arrangement at the Al/$(1\,0\,\bar{1}\,0)TiB_2$ interface, where Fe and Si are co-segregated, was further analysed and quantified using atomic-resolution HAADF-STEM image, as shown in Figure 5(b). The atoms within the extra layers exhibit in-plane ordering. The extra layers formed due to the interfacial

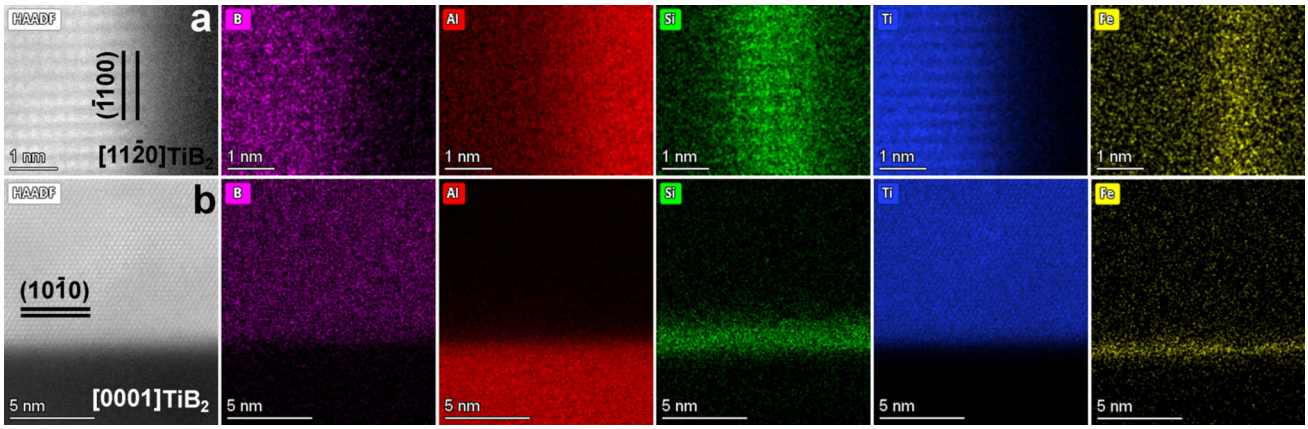

Fig. 4—Elemental segregation at the Al/TiB_2 interface in Al–3.7Ti–1.5B–1.5Fe−1.0Si alloy. (*a*) EDS elemental mapping acquired at the Al/$(\bar{1}100)$ TiB_2 interface along $[11\bar{2}0]TiB_2$ direction, showing Ti (blue), Al (red), Si (green), and Fe (yellow), and (*b*) EDS elemental mapping of the Al/$(10\bar{1}0)$ TiB_2 interface acquired along $[0001]TiB_2$ direction, showing Ti (blue), Al (red), Si (green), and Fe (yellow) (Color figure online).

segregation was considered as the segregation 2DC. The zigzag configuration of these layers is coherent with the TiB_2 lattice, with the interlayer spacings measured as 0.32 ± 0.007 and 0.26 ± 0.005 nm. Notably, the spacing between the outermost Ti layer and the top segregation layer is 0.30 ± 0.01 nm or 0.15 ± 0.005 between each single layer in the segregation 2DC, compared to 0.26 nm, the *d*-spacing of $(\bar{1}100)TiB_2$ planes.

The atomic structure resulting from Fe and Si co-segregation at the Al/$(10\bar{1}0)TiB_2$ interface is also clearly visible when viewed along $[0001]$ direction of TiB_2, as shown in Figure 5(d). Figure 5(d) shows the three extra layers with a zigzag configuration observed above the outermost Ti layer. These layers remain coherent with the TiB_2 lattice, with interlayer spacings measured as 0.31 ± 0.005 nm. Notably, the spacing between these segregated layers is consistent with that observed along $[11\bar{2}0]$ direction of TiB_2: 0.304 ± 0.005 nm, larger than the typical 0.26 nm, the spacing of $(\bar{1}100)$ planes of TiB_2.

The presence of Fe and Si within this 2 to 3 layers 2DC was previously confirmed by EDS mapping, as shown in Figures 4(a) and (b). The intensity profile in Figure 3(h) clearly displays the Si and Fe signal. Figure 5(e) presents the intensity profile extracted along the third 2DC layer in the STEM image [Figure 5(a), white arrow], illustrating the variation in signal intensity. The profile reveals a well-ordered region extending to approximately the midpoint, beyond which the signal becomes increasingly disordered and noisy, indicating a loss of structural order. This behaviour demonstrates the transition of the 2DC structure from three layers to two layers.

C. *Interfacial Segregation of Si at the Al/(0 0 0 1) TiB_2 Interface*

In contrast to the $(\bar{1}100)TiB_2$/Al interface, Si is the only element that segregates at the Al/(0 0 0 1) TiB_2 interface. Previous studies have demonstrated that an Al_3Ti 2DC can form above the (0 0 0 1) TiB_2 surface in Al–Ti–B master alloys with excess Ti, such as Al–5Ti–1B.[3] However, in alloys with Si concentrations exceeding 3 wt pct, Si segregation at the Al/(0 0 0 1) TiB_2 interface disrupts the pre-existing Al_3Ti 2DC by forming a two-dimensional solution (2DS), a phenomenon commonly referred to as poisoning. Despite its recognition, the dynamic nature of this poisoning process remains insufficiently understood due to the lack of direct empirical evidence.

In the present study, the Al–3.7Ti–1.5B–1.5Fe−1.0Si master alloy, which contains excess Ti but a Si concentration below the critical 3 wt pct threshold, was subjected to an extended treatment duration (4 hours), in contrast to the conventional poisoning process typically completed within 20 minutes. A transitional dynamic process was observed, which is presented in Figure 6.

Figure 6 presents high-resolution HAADF-STEM images of the Al/(0 0 0 1) TiB_2 interface, viewed along the $[11\bar{2}0]$ and $[10\bar{1}0]$ directions of TiB_2. An uneven formation of a 2DC was observed on top of the TiB_2 surface, varying in thickness from one to two atomic layers. A two-layer structure is generally the most common configuration, suggesting preferential segregation behaviour. However, the variation in brightness of the second layer suggests compositional fluctuations, likely due to varying concentrations of Al, Si, and Ti, as shown in Figures 6(d) and (f), which may result from different formation mechanisms or from poisoning/dissolution processes. Figure 6(a) clearly reveals two bright layers above the (0 0 0 1) TiB_2 surface along the $[11\bar{2}0]$ zone axis, a feature that has never been reported. The variation in planar spacing within these segregated 2DC layers and the TiB_2 lattice is measured and shown in Figure 6(d). It is evident that this segregated 2DC is coherent with the TiB_2, with a smaller interplanar spacing of 0.23 ± 0.003 nm between the (0 0 0 1) planes, compared to the 0.32 ± 0.005 nm spacing between two adjacent Ti layers in TiB_2. The observed atomic arrangement is similar to the previously

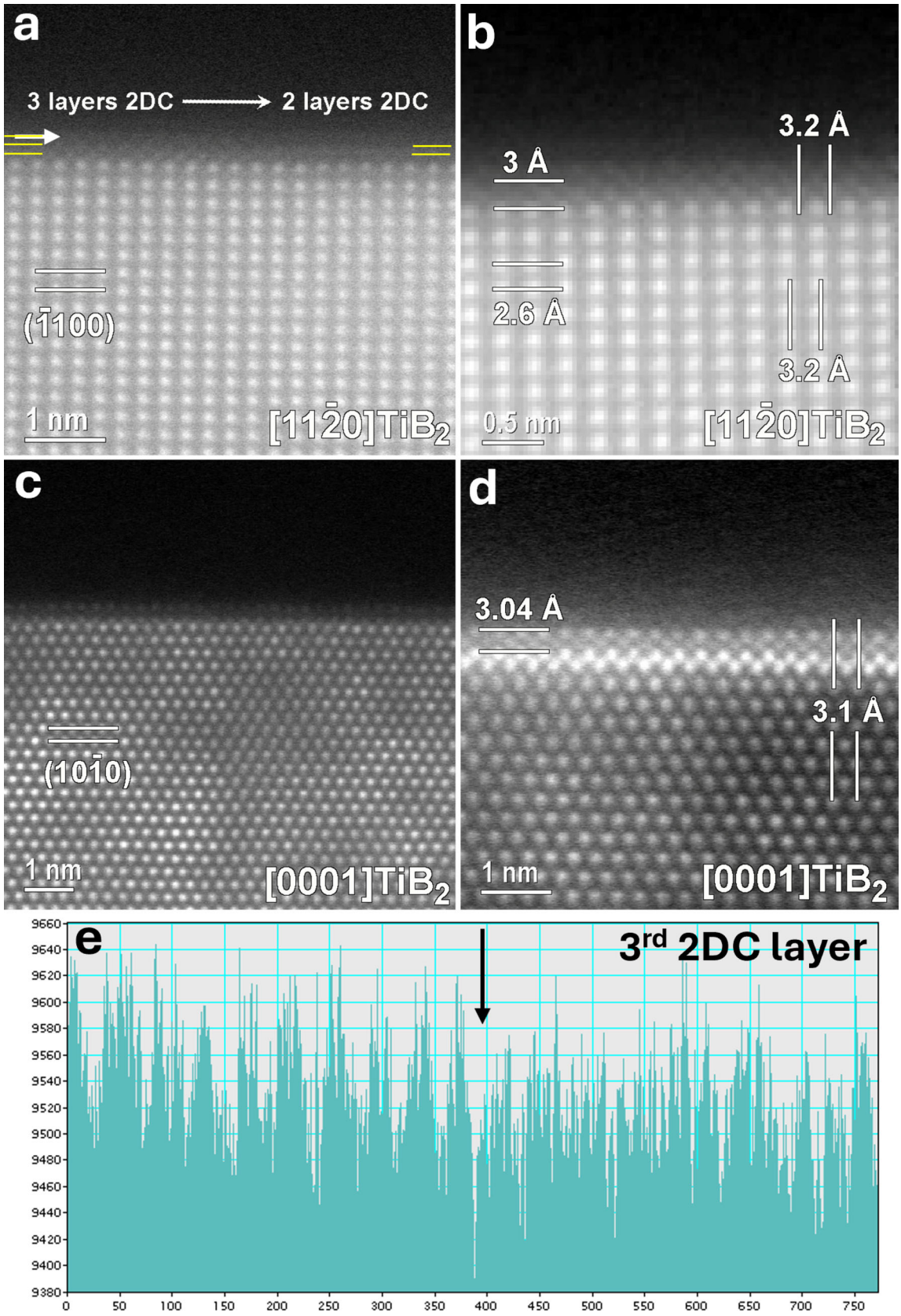
a
3 layers 2DC
2 layers 2DC
(1̄100)
1 nm
[11̄20]TiB2
b
3.2 Å
3 Å
2.6 Å
3.2 Å
0.5 nm
[11̄20]TiB2
c
(10̄10)
1 nm
[0001]TiB2
d
3.04 Å
3.1 Å
1 nm
[0001]TiB2
e
3rd 2DC layer
9660
9640
9620
9600
9580
9560
9540
9520
9500
9480
9460
9440
9420
9400
9380
0
50
100
150
200
250
300
350
400
450
500
550
600
650
700
750

◀Fig. 5—Atomic-level HAADF-STEM analysis of the Al/TiB_2 interface recorded along $[1\,1\,\bar{2}\,0]$ and $[0\,0\,0\,1]TiB_2$ directions. (*a*) HAADF-STEM image showing the atomic arrangement of Fe and Si co-segregation at the Al/$(\bar{1}\,1\,0\,0)$ TiB_2 interface viewed along the $[1\,1\,\bar{2}\,0]$ TiB_2 direction, and (*b*) zoomed-in image with corresponding measured planar spacings. (*c*) HAADF-STEM image showing the atomic arrangement of Fe and Si co-segregation at the Al/$(1\,0\,\bar{1}\,0)$ TiB_2 interface viewed along $[0\,0\,0\,1]TiB_2$ direction and (*d*) zoomed-in image with corresponding measured planar spacings. (*e*) Intensity profile extracted along the 3rd 2DC layer in the STEM image a (white arrow), illustrating the variation in signal intensity. The profile reveals a well-ordered region extending to the midpoint, beyond which the signal becomes highly disordered and noisy, indicating a loss of structural order.

reported Al_3Ti 2DC[3] although one additional layer can be clearly seen. Figure 6(b) shows a localized region where the 2DC transitions from a two-layer to a single-layer structure. In contrast, Figure 6(c) presents a region featuring a single, bright, in-plane ordered layer within the 2DC, along with a less visible second layer. Although three distinct conditions of interfacial Si segregation at the Al/(0 0 0 1) TiB_2 interface are observed, Figure 6(c), considered as single Al_3Ti 2DC layer, is the most commonly encountered configuration in this sample. In contrast, Figure 6(a), which depicts two bright segregation layers, is less frequently observed, while the transitional state shown in Figure 6(b) typically precedes the configuration in Figure 6(a). Figure 6(g) presents the overlapping intensity profiles extracted along the white arrows in the HAADF-STEM of Figure 6(b), showing the variation in the 2nd 2DC layer intensity.

The effect of the interfacial segregation of Si at Al/(0 0 0 1) TiB_2 interface was examined through viewing along the $[1\,0\,\bar{1}\,0]TiB_2$ direction, as shown in Figures 6(e) and (f). It can be seen that the first segregation layer with similarity of Al_3Ti 2DC can be clearly seen at the top of the Ti layer. The second layer is less bright and visible although it becomes visible when changing the contrast and brightness, which are different to the observed case as shown in Figure 6(a). It also demonstrates the low fraction of Ti atoms in the second layer.

IV. DISCUSSION

A. *Segregation Phenomenon at Al/TiB_2 Interfaces*

HAADF–STEM imaging and EDS analysis in Figures 2, 3, and 4 have revealed Si segregation at the Al/(0 0 0 1), and Al/$(\bar{1}\,1\,0\,0)TiB_2$ interfaces, and the co-segregation of Fe and Si at the Al/$(\bar{1}\,1\,0\,0)TiB_2$ interface. The co-segregation of Fe and Si has resulted in the formation of multiple interfacial layers (generally 2 layers), which are in-plane ordered. Usually, elemental segregation behaviour at an interface can be primarily assessed in terms of atomic interactions based on the bonding of these atoms involved at the interfaces. In the Al–Ti–B master alloy of this study, Al, Fe, Si, and Ti atoms, plus those common impurities such as Mn and Ni, are expected to compete for segregation at the interfaces. The competition can be primarily anticipated by comparison of the mixing enthalpies (ΔH^{mix}) between these atoms. It has been reported that ΔH^{mix}_{Ti-Mn}, ΔH^{mix}_{Ti-Fe}, ΔH^{mix}_{Ti-Al}, ΔH^{mix}_{Ti-Ni}, ΔH^{mix}_{Ti-B}, and ΔH^{mix}_{Ti-Si} are − 8, − 17, − 30, − 35, − 58, and − 66, kJ/mol, respectively,[23] while ΔH^{mix}_{B-Al}, ΔH^{mix}_{B-Si}, ΔH^{mix}_{B-Ni}, ΔH^{mix}_{B-Fe}, ΔH^{mix}_{B-Mn} , and ΔH^{mix}_{B-Ti} are 0, − 14, − 24, − 26, − 32, and − 58, kJ/mol, respectively.[23] Among these values, Si has the most negative mixing enthalpy with Ti and thus is expected to have the largest potential to interact with those Ti atoms on TiB_2 surface. This is apparently consistent with the experimental observation that Si segregates on all the TiB_2 surfaces which terminated with corresponding Ti planes. It is therefore believed that Si segregation on all the terminated TiB_2 surface is attributed to its strong interaction with Ti atoms. The mixing enthalpy values are − 17 and − 26 kJ/mol for Fe–Ti and Fe–B, respectively, suggesting a stronger interaction between Fe and B than that between Fe and Ti. According to the crystal structure of TiB_2 (ICSD-COLLCODE 56723),[24] those B atoms close to the interface are beneath the outermost (0 0 0 1) Ti layer of TiB_2 and fully bonded with Ti atoms. However, B atoms on $\{1\,0\,\bar{1}\,0\}TiB_2$ surfaces are unsaturated, providing the opportunity for Fe to be attracted to the B atoms. This is consistent with the experimental results that, rather than on (0 0 0 1)TiB_2 surface, Fe segregates only on the $(\bar{1}\,1\,0\,0)TiB_2$ surface where unsaturated B atoms are available. In contrast, the Fe segregation on the (0 0 0 1)TiB_2 is difficult to achieve under present experimental conditions.

The interfacial segregation of alloying elements depends on many factors, including alloy composition, segregation time, holding temperature, *etc*. These factors interact with each other and influence the extent and behaviour of segregation at the interface. Despite the more negative mixing enthalpy (− 32 KJ/mol) between B and Mn than that between B and Fe (− 26 KJ/mol), Mn segregation was not observed at the interface in this work, likely due to the significantly lower concentration of Mn which is at the impurity level (0.1 pct) compared to Fe 1.5 pct as shown in Table I. This demonstrates that the concentration of an alloying element plays an important role in determining its segregation behaviour.

B. *Nature of Segregation Layers at Al/$(\bar{1}\,1\,0\,0)TiB_2$ Interface*

Experimental results (Figures 5 and 6) show that the interfacial layers formed by co-segregation of Fe and Si exhibit distinct characteristics:

(1) the variable two atomic layers are in-plane ordered; Further examination will focus solely on the two-layer 2DC structure, based on its general segregation behaviour.
(2) the 2 layers are a 2-dimensional compound (2DC) rather than a 3-dimensional bulk phase;
(3) the 2DC layers contain at least Fe and Si or even Al based on the EDS results (Figures 2, 3, 4, and

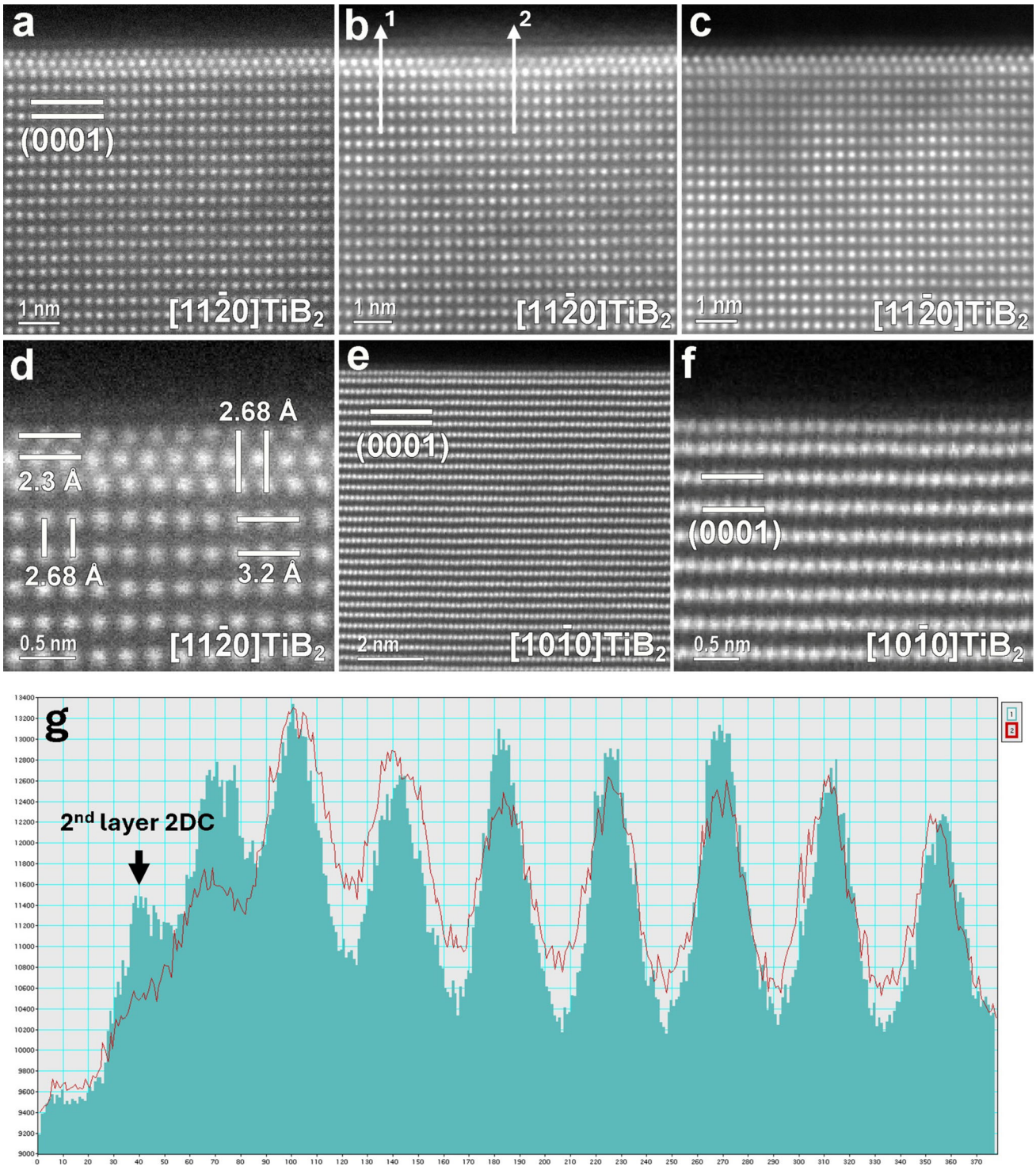

Fig. 6—High-resolution HAADF-STEM analysis across the Al/TiB_2 interface viewed along the $[1\,1\,\bar{2}\,0]$ and $[1\,0\,\bar{1}\,0]TiB_2$ directions. (*a*) through (*c*) HAADF-STEM images showing the transition processing from 2 layers of 2DC atomic arrangement with Ti and Si co-segregation at Al/$(0\,0\,0\,1)TiB_2$ interface viewed along $[1\,1\,\bar{2}\,0]$ TiB_2 direction, (*d*) the measured planar spacings of the 2 layers 2DC atomic arrangement above the $(0\,0\,0\,1)TiB_2$ surface, and (*e*) and (*f*) the atomic arrangement with Ti and Si co-segregation at Al/$(0\,0\,0\,1)TiB_2$ interface viewed along $[1\,0\,\bar{1}\,0]TiB_2$ direction, (*g*) overlapping intensity profiles extracted along the white arrows in the HAADF-STEM image (b), showing the variation in the 2nd 2DC layer intensity.

5), potential involvement of Ti, Mn, Zn, and Ni in the 2DC ruled out (Figure 2).

It is noteworthy that the segregated 2DC at the Al/$(\bar{1}\,1\,0\,0)TiB_2$ interface closely resembles the co-segregated 2DC of Fe and Si at the Al/$(1\,0\,\bar{1}\,0)$ AlB_2 interface, as previously reported,[22] in terms of both elemental composition and interlayer spacings.

The potential crystal structure of the 2DC is investigated based on the different crystal structures of various AlFeSi compounds well documented in the ICSD database. For most of AlFeSi compounds, Si atoms share their atomic sites with Al atoms with different occupancy, indicating that the concentration and site of Si atoms in those AlFeSi compounds are flexible and variable.[25–30] Only in a few AlFeSi compounds, such as δ-Al_4FeSi_2, with higher Si concentration, feature Si atoms occupying independent atomic site with 100 pct occupancy.[29] In AlFeSi compounds, Fe sites are not shared with Al or Si, but can be shared with transition elements such as Mn and Cr.

The segregation layers (2DC) at Al/$(\bar{1}\,1\,0\,0)$TiB$_2$ when viewed along the $[1\,1\,\bar{2}\,0]$ direction of TiB_2 particle are shown in Figures 5(a) and (b). They show that the in-planar ordered Fe and Si co-segregation layers are slightly darker than the Ti layers of TiB_2 in the HADDF image. Pure Fe (Z = 26) columns should generally appear brighter than pure Ti (Z = 22) ones due to its higher atomic number. The slightly lower brightness of the Fe-segregation layer is apparently due to chemical composition or edge effect, indicating that the atomic layer between the observed Fe-segregation layers may contain higher concentration of Al/Si, contributing to a darker appearance. No periodic contrast variation with alternating bright and dark atomic columns, characteristic of Al_3Ti 2DC[3] and Al_3Zr 2DC,[21] is observed, indicating that Fe atoms within the segregated 2DC are uniformly distributed when viewed along the $[1\,1\,\bar{2}\,0]$ zone axis of the TiB_2 particle.

The spacing between the first layer of the 2DC and the top Ti layer of the TiB_2 substrate is measured to be 1.5 ± 0.05 Å. The same spacing, 1.5 ± 0.05 Å, is observed between the first and second layers of the 2DC. Consequently, the total distance from the terminated $(\bar{1}\,1\,0\,0)$ plane of TiB_2 to the second layer of the 2DC is 3.0 ± 0.1 Å, which is slightly larger than the interplanar spacing of the $(\bar{1}\,1\,0\,0)$ planes in TiB_2 (2.6 Å).

Despite this difference, the segregation layers remain coherently matched with the $(\bar{1}\,1\,0\,0)$TiB$_2$ plane. The spacing between atomic columns within the interfacial layer along the [0 0 0 1] TiB_2 direction is measured to be 3.2 Å, exactly matching the d-spacing of the (0 0 0 1) TiB_2 planes.

The structure and chemistry of the AlFe(Si) 2DC at the Al/$(1\,0\,\bar{1}\,0)$ TiB_2 interface exhibit three distinct features:

1. A zigzag atomic arrangement along a specific crystallographic direction.
2. Each atomic column contains a uniform distribution of Al/(Al + Si) and Fe atoms when viewed along the $[1\,1\,\bar{2}\,0]$ direction of the TiB_2 particle.
3. A planar spacing of 3.2 Å within the 2DC.

Following a detailed examination of various Al–Fe and Al–Fe–Si compounds in the ICSD database, only one structure was found to fully match the characteristics of the observed 2DC at the Al/$(1\,0\,\bar{1}\,0)$ TiB_2 interface. This compound is the high-temperature ε-Al_8Fe_5 phase (ICSD Collection Code: 165163), which, with slight adjustments to its lattice parameters, aligns well with the experimentally observed segregation configuration.

The ε-Al_8Fe_5 phase crystallizes in a body-centred cubic (bcc) structure of the Hume-Rothery Cu_5Zn_8-type, with space group $I\bar{4}3m$ (No. 217), Z = 4, Pearson symbol *cI52*, and Strukturbericht designation *D82*. The reported lattice parameter is $a = 8.9757(2)$ Å.[31]

As illustrated in Figure 7(a), the unit cell of ε-Al_8Fe_5 consists of atomic layers with varying atomic arrangements and Fe concentrations. Notably, the top, middle, and bottom layers exhibit identical atomic configurations with relatively higher Fe content compared to the other repeating building blocks (highlighted with red dotted frames in the figure). These layers are referred to hereafter as higher Fe concentration layers.

It also shows that there are two repeated building blocks in the unit cell, as marked by the red dotted rectangles in Figure 7(a). In each of the building blocks, there are two layers where the atomic arrangement is close to a zigzag fashion when viewed in [1 0 0] direction of ε-Al_8Fe_5 phase. The atomic ratio of Al and Fe for every atomic column in this direction is 2:1, *i.e.* Al and Fe atoms distribute evenly in the columns. This is the same as the 2DC formation on the Al/(0 0 0 1) AlB_2 reported in previous work.[22]

The lattice relaxation from the ε-Al_8Fe_5 phase to the proposed Al_8Fe_5 2DC structure is illustrated in Figure 7, transitioning from (b, c) to (d, e), which show the side view and the (0 0 1) plane projection, respectively. When viewed along the [0 1 0] direction, the atomic ratio of Al to Fe is observed to be 2:1, consistent with the composition of the ε-Al_8Fe_5 phase.

The planar spacings of the 2DC building block are 3.0 Å along the (0 0 1) planes and 1.5 Å along the (1 0 0) planes, values that closely approximate the experimentally measured spacings of 3.2 and 1.5 Å, respectively, for the segregation layers at the TiB_2 surface. It is noteworthy that the atomic positions of Al and Fe within the unit cell are slightly displaced from perfect linear alignment, indicating subtle relaxation.

Fe interfacial segregation likely occurs at elevated temperatures, resulting in the formation of this distinct 2DC structure comprising several atomic layers. Given the strong structural templating effect imposed by the underlying $TiB_2(\bar{1}\,1\,0\,0)$ surface, it is reasonable to assume that the Al and Fe atoms at the interface undergo slight positional relaxation to achieve coherent alignment with the TiB_2 lattice.

As schematically shown in Figure 7(d), this results in an Fe-rich segregation layer where Al and Fe atoms adjust their positions to match the atomic registry of the Al atoms in the TiB_2 prismatic plane, as further illustrated in Figures 7(d) and (e). The resulting Al_8Fe_5 2DC model aligns well with the experimentally observed structure and chemistry of the Fe-rich segregation layers seen on the prismatic TiB_2 surface [refer to Figure 5(b)].

Figures 8(a) and (b) schematically illustrate the lattice matching between the Al_8Fe_5 2DC and TiB_2 when viewed along the $[1\,1\,\bar{2}\,0]$ and [0 0 0 1] directions of TiB_2,

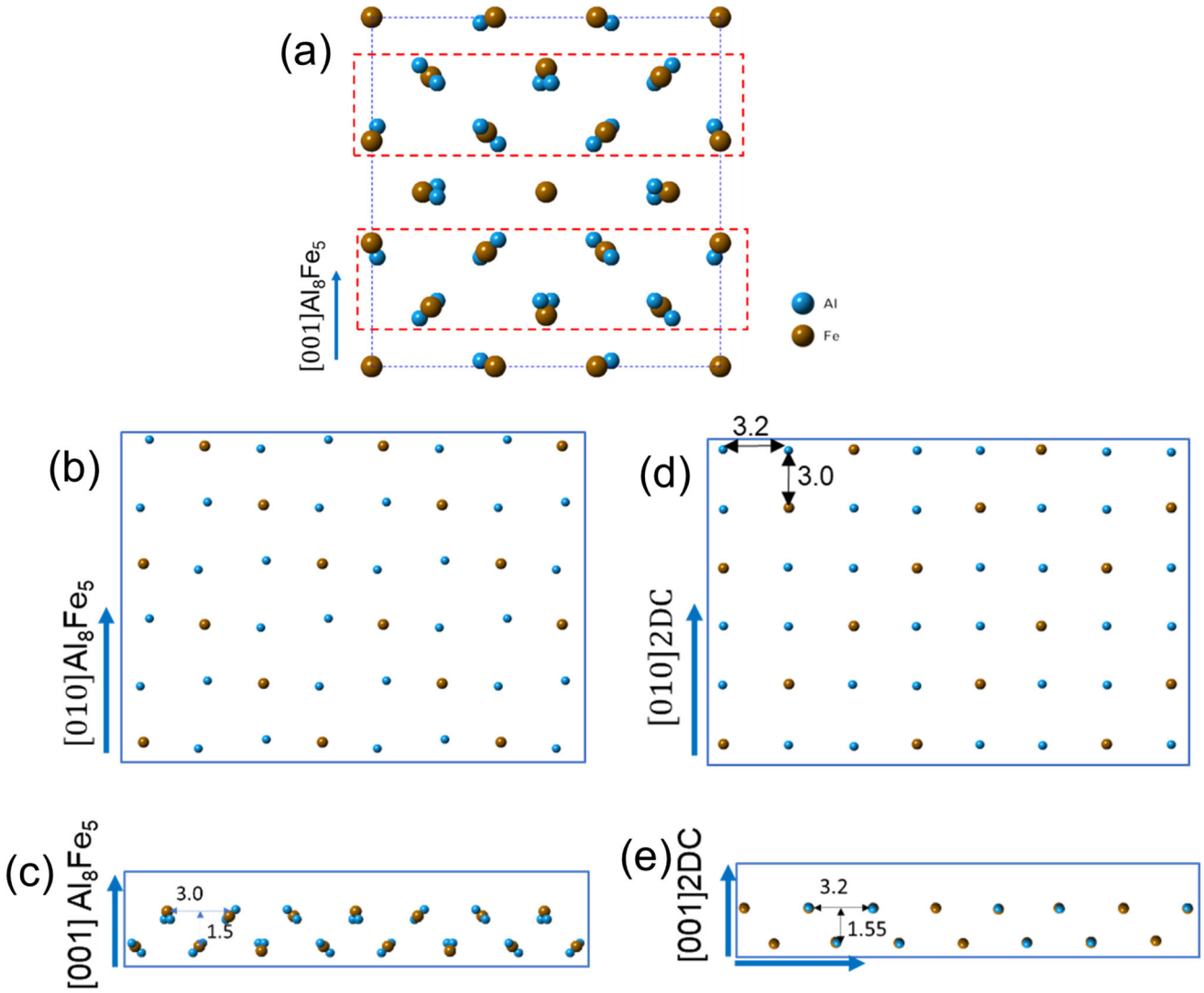

Fig. 7—(*a*) Unit cell of bulk Al_8Fe_5 showing higher Fe concentration in the top, bottom, and middle (001) layers, and lower and evenly distributed Fe in the building blocks (marked with red dotted frames); (*b*) projection of (001) plane (one layer) in 2DC building block of Al_8Fe_5, and (*c*) side view of the 2DC block (two layers) of Al_8Fe_5; (*d*) projection of (001) plane (one layer) of 2DC pseudo Al_8Fe_5, and (*e*) side view of the 2DC pseudo Al_8Fe_5 (two layers). (make the annotation the same font style, either times new roman or arial) (Color figure online).

respectively, based on the following orientation relationship (OR):

$$(10\bar{1}0)[11\bar{2}0]\mathrm{TiB_2}//2\mathrm{DC}\ (001)[100]\mathrm{Al_8Fe_5}2\mathrm{DC} \quad [\mathrm{OR1}]$$

In contrast to our previous study, where the Al_8Fe_5 2DC was identified at the $(\bar{1}100)$ AlB_2 interface and could only be observed along the $[11\bar{2}0]$ AlB_2 zone axis due to limitations in TEM operation, this study allows for a clearer observation of the same Al_8Fe_5 2DC along both the $[11\bar{2}0]$ and [0 0 0 1] directions of TiB_2. The interface matching models described above were rotated to align with these two different zone axes, further enhancing both our previous and current findings, as shown in Figures 8(a) and (b). It is evident that Figures 8(a) and (b) align well with Figures 5(a) and (c), providing a second confirmation of our previous discovery with new evidence.

The similarity in the interfacial segregation of Fe at the $(\bar{1}100)$ planes of both TiB_2 and AlB_2 can be attributed to the unsaturated B-bonding at the interfaces. In both TiB_2 and AlB_2, the B atoms have incomplete coordination with neighbouring atoms, creating a favourable environment for Fe segregation. This unsaturation of B-bonds provides sites for Fe to accumulate, contributing to its interfacial segregation. In contrast, the segregation of Si at the interface is primarily driven by the strong covalent bonding between Ti and Si. The Ti–Si bond is particularly stable, leading to the preferential segregation of Si at the Al/$(10\bar{1}0)$ TiB_2 interface. The relative strength of these interactions results in distinct segregation behaviours for Fe and Si, with Fe tending to segregate at the B-rich sites and Si being more strongly bound to Ti atoms. These

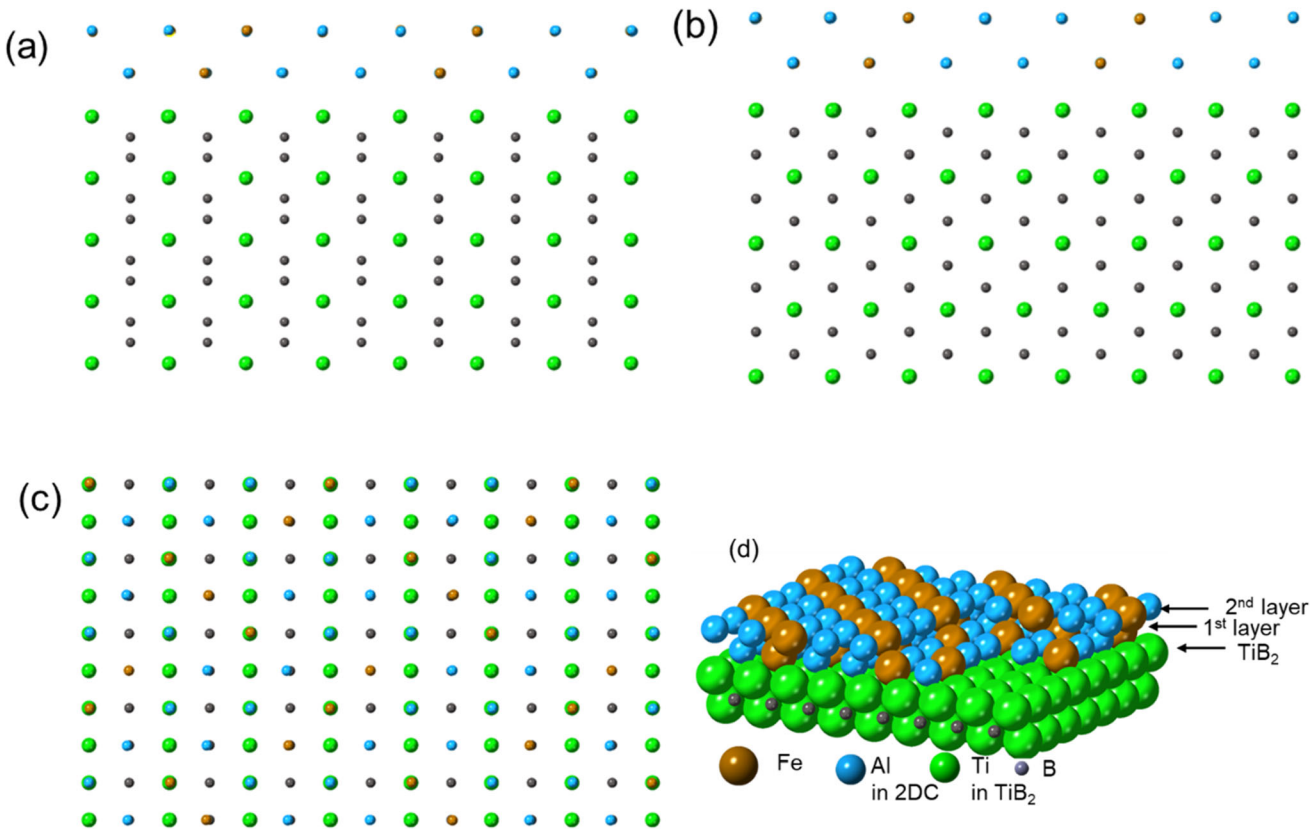

Fig. 8—Schematic illustration showing (*a*) the Al_8Fe_5 2DC on the top of the $(1\,0\,\bar{1}\,0)$ TiB_2 viewed along the $[1\,1\,\bar{2}\,0]$ zone direction of TiB_2, (*b*) the Al_8Fe_5 2DC on the top of the $(1\,0\,\bar{1}\,0)$ TiB_2 viewed along the [0 0 0 1] zone direction of TiB_2, (*c*) the planar matching between the first layer of 2DC and the top Al layer at $(1\,0\,\bar{1}\,0)$ TiB_2, and (*d*) the 3D construction of the Al_8Fe_5 2DC on the top of the TiB_2 according to the OR: $(1\,0\,\bar{1}\,0)[1\,1\,\bar{2}\,0]TiB_2$// (0 0 1) [1 0 0] Al_8Fe_5 2DC.

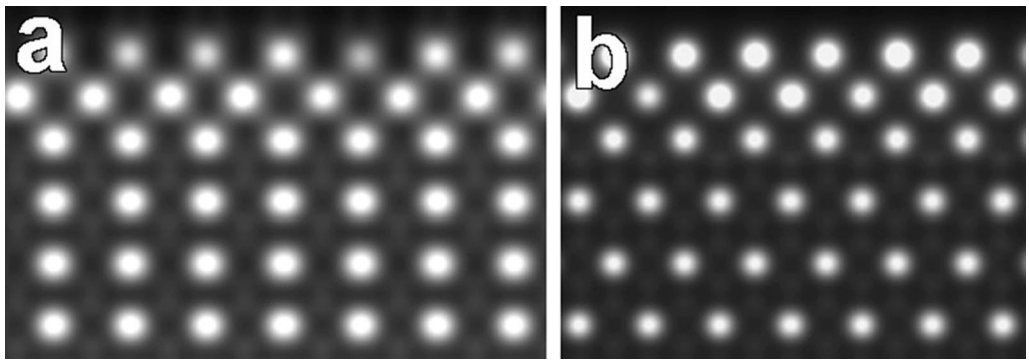

Fig. 9—Simulated HADDF-STEM images along the (*a*) $[1\,1\,\bar{2}\,0]$ of the TiB_2, and (*b*) [0 0 0 1] of TiB_2 directions. The simulated images correspond to the constructed Al_8Fe_5 2DC on the surface of the $(1\,0\,\bar{1}\,0)$ of TiB_2.

differences highlight the role of bonding characteristics in governing the interfacial segregation processes at the TiB_2 and AlB_2 interfaces.

Simulation of atomic-resolution HAADF-STEM images was performed using the commercial software Tempas, in order to validate the established characteristics of the segregation layers, as shown in Figure 9. It shows that the simulation HAADF between the Al_8Fe_5 2DC and TiB_2 followed the OR1 when viewed along both $[1\,1\,\bar{2}\,0]$ and [0 0 0 1] directions of TiB_2 match well with the experimental observation as Figures 5(a) and (c).

Although the structural analysis of the interfacial 2DC matches Al_8Fe_5, it is well established that Si can partially substitute Al sites in Fe-containing intermetallic compounds.[32] Therefore, it is reasonable to propose that the interfacial 2DC is Fe-Si-Al rich (STEM-EDS mapping evidence, Figures 2, 3, and 4), but with the structural similar to Al_8Fe_5 with Si incorporation. This

highlights the cooperative role of Fe and Si in stabilizing interfacial structures.

Compared to the Fe and Si segregation on the TiB_2 in this study and on the AlB_2,[22] the results demonstrated that they have the same interfacial segregation on the $(\bar{1}100)$ crystallographic planes of TiB_2/AlB_2 particles and forms the same (Si incorporated 2DC-Al_8Fe_5) layer at the $Al/(\bar{1}100)TiB_2/AlB_2$ interface. However, the segregation behaviour on the (0 0 0 1) plane is distinctly different. It is known that both TiB_2 and AlB_2 have very similar/almost same crystal structure. However, the chemical conditions such as atomic bonding between Al/B and Ti/B at the faceted interface are different, which are important in changing the interfacial segregation. As discussed above, the unsaturated B at the $Al/(\bar{1}100)TiB_2$ is the key factors to attract the Fe segregation. The Fe segregation is the major reason in formation of the 2DC-Al_8Fe_5 layer. This indicated that the critical factors for the interfacial segregation of Fe are the unsaturated B. This contributes to an important understanding that once the structural templating at the substrates maintains same, the interfacial segregation depends on the strongest chemical factors such as B, highlighting a potentially universal segregation mechanism across different boride substrates. The Ti-deficient and Ti-rich Al–Ti–B master alloys contain two distinct boride phases, AlB_2 and TiB_2, which exhibit different interfacial templating behaviours: Al_3Ti 2DC/(0 0 0 1)TiB_2[3] and clean Al/(0 0 0 1)AlB_2,[22] respectively. Consequently, they can be applied to different alloy systems. For example, AlB_2 is particularly effective in high-Si Al alloys, where it helps resist Si poisoning. Currently, grain refiner development of Al–Ti–B system is mainly focussed on utilizing the interfacial segregation at the Al/(0 0 0 1)Ti/AlB_2 such as Al_3Ti 2DC. Little attention has been paid to the investigation of elemental segregation at the $Al/(\bar{1}100)TiB_2$ or AlB_2 interface. This study offers new scientific insight by revealing the different behaviours of Fe and Si on TiB_2 and AlB_2 in these two distinct master alloys. It also contributes to a deeper understanding of grain refinement mechanisms and opens new pathways for tailoring the performance of grain refiners in aluminium alloys.

C. *Nature of Si Segregation Layers at* $Al/(0001)TiB_2$ *Interface*

The previous study[3] confirmed the formation of an Al_3Ti 2DC on the $Al/(0001)TiB_2$ interface, based on the observation of a single-ordered atomic layer viewed along the $[11\bar{2}0]$ and $[10\bar{1}0]$ directions of TiB_2. In contrast, the present work, for the first time, reveals two Ti-rich segregation layers forming a 2DC structure have been observed at the $Al/(0001)TiB_2$ interface, as shown in Figure 6(a). The atomic arrangement within this bilayer 2DC was carefully analysed in terms of interatomic spacings and composition, and compared with the previously reported results.[3]

The schematics in Figure 10 illustrate the interface between the two Al_3Ti 2DC layers and the $(0001)TiB_2$ substrate, based on the orientation relationship (OR): $(112)[\bar{2}01]$ $Al_3Ti//(0001)[11\bar{2}0]TiB_2$, as shown in Figures 10(a) and (d). The identification of the second Al_3Ti layer further substantiates the formation of the Al_3Ti 2DC at the interface.

EDS mappings (Figures 2 and 3) not only confirmed Si segregation at the Al/(0 0 0 1) TiB_2 interface but also revealed a dynamic process involving the partial dissolution of the second layer of the Al_3Ti 2DC. This observation suggests the onset of dissolution of the first layer of Al_3Ti, a phenomenon referred to as the poisoning process.

It has been previously demonstrated[4] that Si segregation at Al/TiB_2 interface results in eventual breakdown of the performed Al_3Ti 2DC on the (0 0 0 1) TiB_2 surface, leading to the formation of 2D solution layer which has no in-plane order. It was also shown that dissolution of Al_3Ti 2DC becomes noticeable when Si concentration in the alloy exceeds 3 wt pct, and the dissolution rate increases with increasing Si concentration.

The dissolution of Al_3Ti 2DC leads to a reduction in the nucleation potency of TiB_2 particles, a phenomenon known as Si poisoning effect. In this study, Si concentration was 1.0 wt pct, lower than the critical threshold of 3.0 wt pct required for fully dissolving the pre-existing Al_3Ti 2DC. However, the extended holding time of 4 hours during the segregation process may also contribute to the dissolution of the Al_3Ti 2DC. Figure 6(c) captures an intermediate state, positioned between the complete formation of a bilayer Al_3Ti 2DC and the full dissolution of its upper second layer.

The dissolution of the Al_3Ti 2DC begins with Si segregation at the TiB_2 interface, which leads to the replacement of atomic positions, including both Al and Ti atoms. Replacement of Al atoms by Si is more likely to occur initially, due to the lower energy barrier involved. However, when the critical Si concentration is reached, requiring greater Si segregation and longer segregation time, Si atoms may also begin to replace Ti atoms. This substitution marks the actual onset of Al_3Ti 2DC dissolution. Despite these atomic substitutions, some in-plane ordering within the affected atomic layer may still persist, which results in a dimmer yet still ordered atomic arrangement observed in the HAADF-STEM image [Figure 6(c)].

The dissolution of the Al_3Ti 2DC is initiated by Si segregation at the TiB_2 interface, where Si atoms begin to substitute atomic positions originally occupied by Al and Ti. The substitution of Al by Si is energetically more favourable, and thus occurs more readily.[32] However, when the local Si concentration reaches a critical threshold, achievable through extended segregation time, Si atoms may also begin to replace Ti atoms. This substation marks the true onset of Al_3Ti 2DC dissolution.

Despite this substitution, some degree of in-plane atomic ordering may persist in the affected layer, resulting in a noticeably darker but still ordered atomic contrast in the HAADF-STEM image [Figure 6(c)]. It is shown that the second layer is less visible in

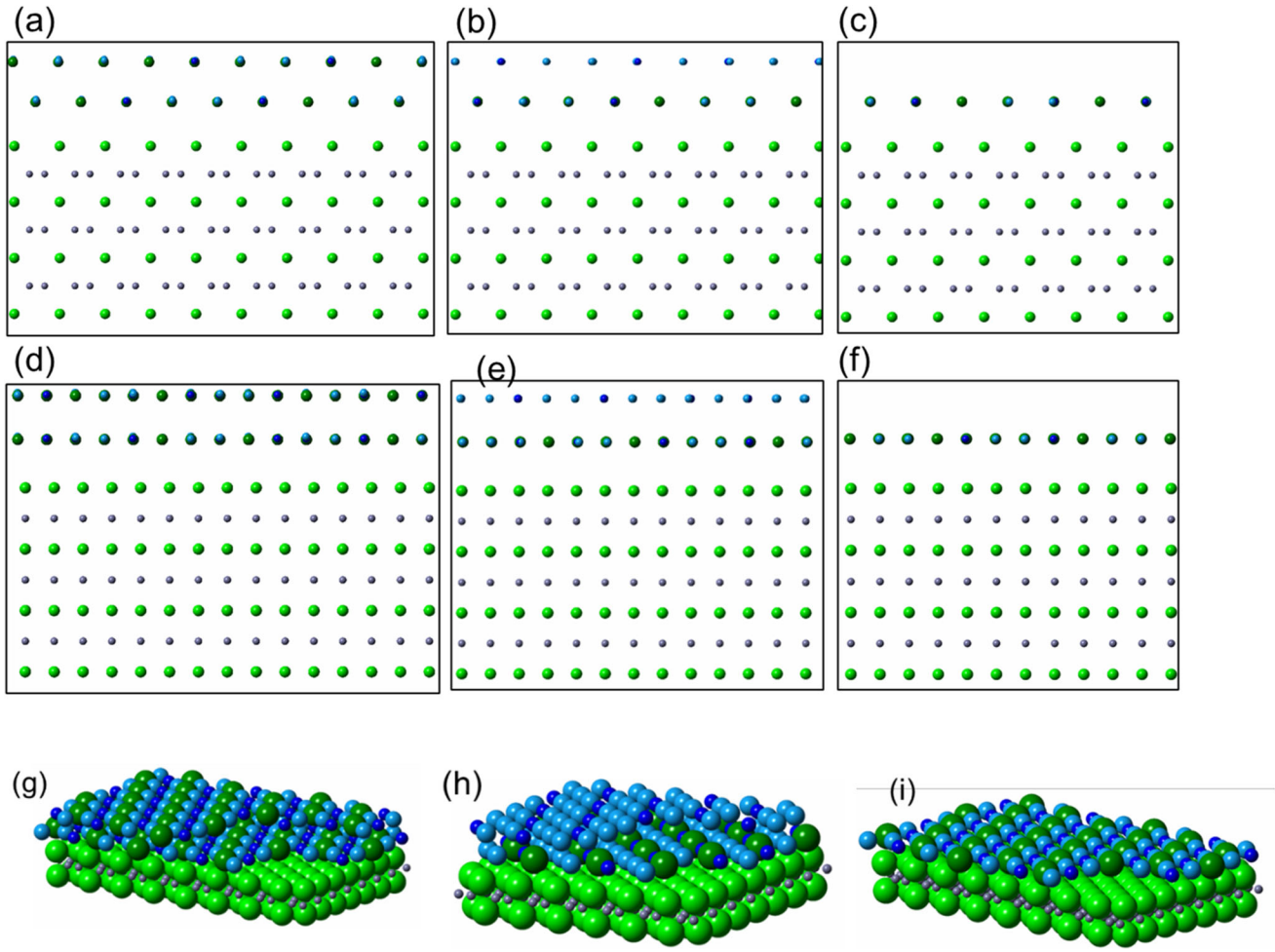

Fig. 10—Schematic illustration showing (*a*) and (*b*) the Si-segregation-modified Al_3Ti 2DC on the top of the $(0\,0\,0\,1)$ TiB_2 when viewed along the $[1\,1\,\bar{2}\,0]$ direction of TiB_2 from 2 layers segregation to 1 layer segregation process, (*d*) through (*f*) the Si-segregation-modified Al_3Ti 2DC on the top of the $(0\,0\,0\,1)$ TiB_2 when viewed along the $[1\,0\,\bar{1}\,0]$ direction of TiB_2 from 2 layers segregation to (*c*) 1 layer segregation process, and (*g*) through (*i*) the 3D construction of the Si-segregation-modified Al_3Ti 2DC on the top of the TiB_2 according to the OR: $(1\,1\,2)[\bar{2}\,0\,1]$-modified $Al_3Ti//(0\,0\,0\,1)[1\,1\,\bar{2}\,0]TiB_2$.

experimental HAADF-STEM image due to the reduced Ti concentration and diminished ordering.

Furthermore, the experimental result in Figure 3(i) also demonstrates that the Ti concentration decreases with increasing distance from the S/L interface. In case of Si poisoning of the Al_3Ti 2DC/$(0\,0\,0\,1)TiB_2$,[4] when the Si concentration in the liquid exceeds 3wt pct, Si segregation provides a further thermodynamic driving force to replace the Ti atomic positions within the Al_3Ti 2DC. This process weakens the overall bonding network of the 2DC and ultimately leads to its complete dissolution. In fact, the observed Si segregation at the Al_3Ti 2DC/TiB_2 interface in this study represents a transition state preceding the complete dissolution of the Al_3Ti 2DC.

Based on above discussion, schematic atomic models were constructed to illustrate the dynamic dissolution process of the second Al_3Ti 2DC layer at the Al_3Ti / $(0\,0\,0\,1)TiB_2$ interface, as shown in Figure 10. The interface was analysed along the $[1\,1\,\bar{2}\,0]$ and $[1\,0\,\bar{1}\,0]$ crystallographic directions of TiB_2. A 3D model of the Si-segregation-modified Al_3Ti 2DC on top of the TiB_2 substrate was also illustrated, based on the orientation relationship (OR): $(1\,1\,2)[\bar{2}\,0\,1]$-modified $Al_3Ti//(0\,0\,0\,1)[1\,1\,\bar{2}\,0]TiB_2$. This is in good agreement with the experimental observations presented in Figure 6.

The HAADF-STEM images simulated along the $[1\,1\,\bar{2}\,0]$and $[1\,0\,\bar{1}\,0]$ directions of TiB_2, based on the constructed atomic models, are presented in Figure 11. The simulated images of the modified Al_3Ti and TiB_2 interface align well with the experimental results in both atomic patterns and intensity contrast, confirming the validity of the constructed models.

V. SUMMARY

(1) Fe segregation occurs only at the Al/$(\bar{1}\,1\,0\,0)TiB_2$ interface, with no Fe segregation being observed on the basal $(0\,0\,0\,1)$ surface of TiB_2. In contrast to Fe, Si segregates not only at the Al/

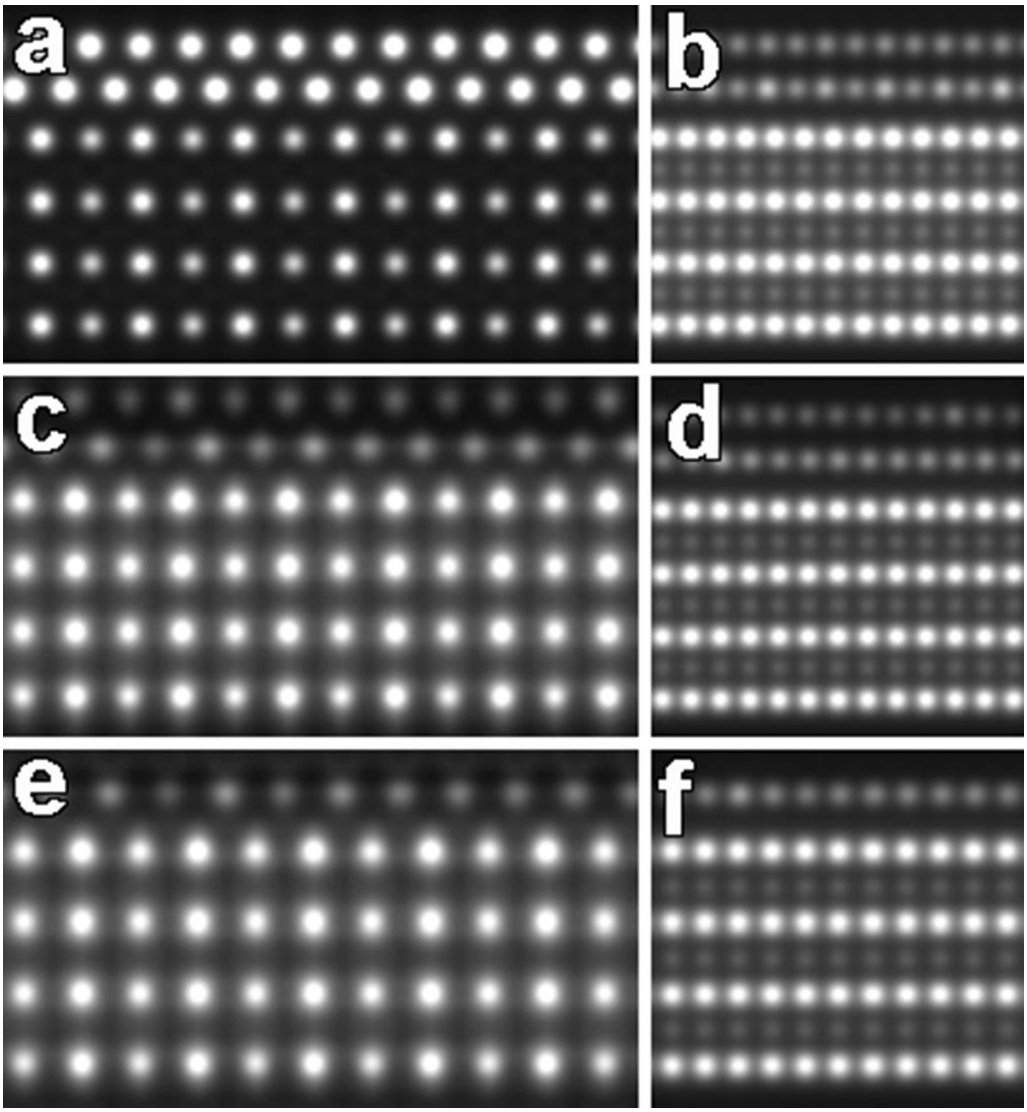

Fig. 11—Simulated HAADF-STEM images of $(0\,0\,0\,1)TiB_2$ when viewed along (*a*) through (*c*) $[1\,1\,\bar{2}\,0]$ and (*d*) through (*f*) $[1\,0\,\bar{1}\,0]$ of TiB_2, showing the Si segregation effect on the evolution of Al_3Ti 2DC from 2 layers to 1 layer on the top of the $(0\,0\,0\,1)$ TiB_2 surface.

$(1\,0\,\bar{1}\,0)TiB_2$ interface but also at the Al/(0 0 0 1)TiB_2 interface, effectively covering all the surfaces of the synthesized TiB_2 particle.

(2) Fe and Si co-segregate at the Al/$(\bar{1}\,1\,0\,0)TiB_2$ interface, resulting in a multiple-layered 2-dimensional compound (2DC), while only Si segregation alone was detected at the Al/(0 0 0 1)TiB_2 interface.

(3) Fe and Si co-segregation was characterized by its crystal structure and chemistry assembling the atomic layers in the unit cell of ε-Al_8Fe_5 phase (body-centred cubic (bcc) structure (Hume-Rothery Cu_5Zn_8-type, (space group $I\,\bar{4}3m$ (No. 217), $Z = 4$, Pearson symbol $cI52$, Strukturbericht designation $D8_2$)) with the lattice parameter being $a = 8.9757(2)$ Å).

(4) The segregation behaviour of Fe and Si and the formation of the 2DC on the Al/$(\bar{1}\,1\,0\,0)TiB_2$ interface in Al–3.7Ti–1.5B–1.5Fe–1.0Si alloy is similar to that on Al/$(\bar{1}\,1\,0\,0)AlB_2$ interface in Al–2.8Ti–1.8B–1.0Fe–1.0Fe–0.5Si alloy.[22]

(5) Experimental observation of the dynamic poisoning process of Al_3Ti 2DC from 2 layer to 1 layer due to the Si interfacial segregation at Al/$(0\,0\,0\,1)TiB_2$ interface. The segregated Si is incorporated into the pre-existing Al_3Ti 2DC forming a new $(Al, Si)_3Ti$ 2DC. The Si segregation at the Al/(0 0 0 1)TiB_2 interface observed in this study is actually a transition state before the eventually dissolution of the pre-existing Al_3Ti 2DC layer when Si content is sufficiently high.

ACKNOWLEDGMENTS

Thanks go to LiME hub of BCAST in Brunel University London. The EPSRC is gratefully acknowledged for providing financial support under Grant EP/N007638/1. This work is also supported by Brunel University London BRIEF award (11937131).

AUTHOR CONTRIBUTIONS

Conceptualization, methodology, Experimental investigation, writing, and review & editing: Z. Q.; Experimental investigation and Reviewing: Y. W.; STEM supports and Reviewing: X.Z. and R. N.; Super STEM supports and Reviewing: R. N. and Q. R; Reviewing support in STEM: S. W.; and Supervision and Funding acquisition: Z. F. All authors have read and agreed to the published version of the manuscript.

FUNDING

This work was financial supported by the EPSRC (UK) for under Grant Number EP/N007638/1 (Future Liquid Metal Engineering Hub). This work is also supported by Brunel University London BRIEF award (11937131).

CONFLICT OF INTEREST

The authors declare no conflict of interest.

OPEN ACCESS

REFERENCES

1. A. Cibula: *J. Inst. Met.*, 1949–50, vol. 76, pp. 321–60.
2. A. Cibula: *J. Inst. Met.*, 1951–52, vol. 80, pp. 1–16.
3. Z. Fan, Y. Wang, Y. Zhang, T. Qin, X.R. Zhou, G.E. Thompson, T. Pennycook, and T. Hashimoto: *Acta Mater.*, 2015, vol. 84, pp. 292–304.
4. Y. Wang, Z. Que, T. Hashimoto, and Z. Fan: *Metall. Mater. Trans. A*, 2020, vol. 51A, pp. 5743–57.
5. M.A. Easton, M. Qian, A. Prasad, and D.H. StJohn: *Curr. Opin. Solid State Mater. Sci.*, 2016, vol. 20, pp. 13–24.
6. O. Engler and J. Hirsch: *Mater. Sci. Eng. A*, 2002, vol. 336, pp. 249–62.
7. Z. Fan: *Int. Met. Rev.*, 2002, vol. 47, pp. 49–75.
8. M.D. Eborall: *J. Inst. Met.*, 1949, vol. 76, pp. 295–320.
9. Y. Birol: *J. Alloys Compd.*, 2009, vol. 486, pp. 219–22.
10. B.S. Murty, S.A. Kori, and M. Chakraborty: *Int. Mater. Rev.*, 2002, vol. 47, pp. 3–29.
11. T.E. Quested: *Mater. Sci. Technol.*, 2004, vol. 20, pp. 1357–69.
12. I. Maxwell and A. Hellawell: *Acta Metall.*, 1975, vol. 23, p. 229.
13. J. Li, F.S. Hage, Q.M. Ramasse, and P. Schumacher: *Acta Mater.*, 2021, vol. 206, p. 116652.
14. D. Wearing, A.P. Horsfield, W.X. Xu, and P.D. Lee: *J. Alloys Compd.*, 2016, vol. 664, pp. 460–68.
15. P. Schumacher, A.L. Geer, J. Worth, P.V. Evans, M.A. Kearns, P. Fisher, and A.H. Green: *Mater. Sci. Technol.*, 1998, vol. 14, pp. 394–404.
16. J.A. Spittle and S.B. Sadli: *Mater. Sci. Technol.*, 1995, vol. 11, pp. 533–37.
17. Y. Wang, S. Wang, Z. Que, C. Fang, T. Hashimoto, X. Zhou, Q.M. Ramasse, and Z. Fan: *Metals*, 2022, vol. 12, p. 1636.
18. Z. Fan: *Metall. Mater. Trans. A*, 2013, vol. 44A, p. 1409.
19. Z. Fan, F. Gao, B. Jiang, and Z. Que: *Sci. Rep.*, 2020, vol. 10, p. 9448.
20. Z. Fan and H. Men: *Metals*, 2022, vol. 12, p. 1547.
21. Y. Wang, C.M. Fang, L. Zhou, T. Hashimoto, X. Zhou, Q.M. Ramasse, and Z. Fan: *Acta Mater.*, 2019, vol. 164, pp. 428–39.
22. Z. Que, Y. Wang, Z. Fan, T. Hashimoto, and X.R. Zhou: *Sci. Rep.*, 2024, vol. 14, p. 8968.
23. A. Takeuchi and A. Inoue: *Mater. Trans.*, 2005, vol. 46, pp. 2817–29.
24. TiB_2-ICSD_CollCode56723.
25. C. Romming, V. Hansen, and J. Gjonnes: *Acta Crystallogr. Sect. B: Struct. Sci.*, 1994, vol. 50, pp. 307–12.
26. J.G. Barlock and L.F. Mondolfo: *Z. Metallkd.*, 1975, vol. 66(10), pp. 605–11.
27. M. Cooper: *Acta Crystall.*, 1967, vol. 23, pp. 1106–07.
28. R.N. Corby and P.J. Blabk: *Acta Crystallogr. Sect. B: Struct. Crystallogr. Cryst. Chem.*, 1977, vol. 33, pp. 3468–75.
29. C. Gueneau, C. Servant, F. d'Yvoire, and N. Rodier: *Acta Crystallogr. Sect. C: Cryst. Struct. Commun.*, 1995, vol. 51, pp. 177–79.
30. V. Hansen, B.C. Hauback, M. Sundberg, C. Romming, and J. Gjonnes: *Acta Crystallogr. Sect. B: Struct. Sci.*, 1998, vol. 54, pp. 351–57.
31. F. Stein, S.C. Vogel, M. Eumann, and M. Palm: *Intermetallics*, 2010, vol. 18, pp. 150–56.
32. C.M. Fang, Z. Que, and Z. Fan: *JOM*, 2024, vol. 77(3), pp. 1091–102.